Cell Reports
Physical Science

Article

Band-gap engineering in Co-/Cu-co-doped ZnO nanorods unlocks superior charge-storage kinetics

Graphical abstract

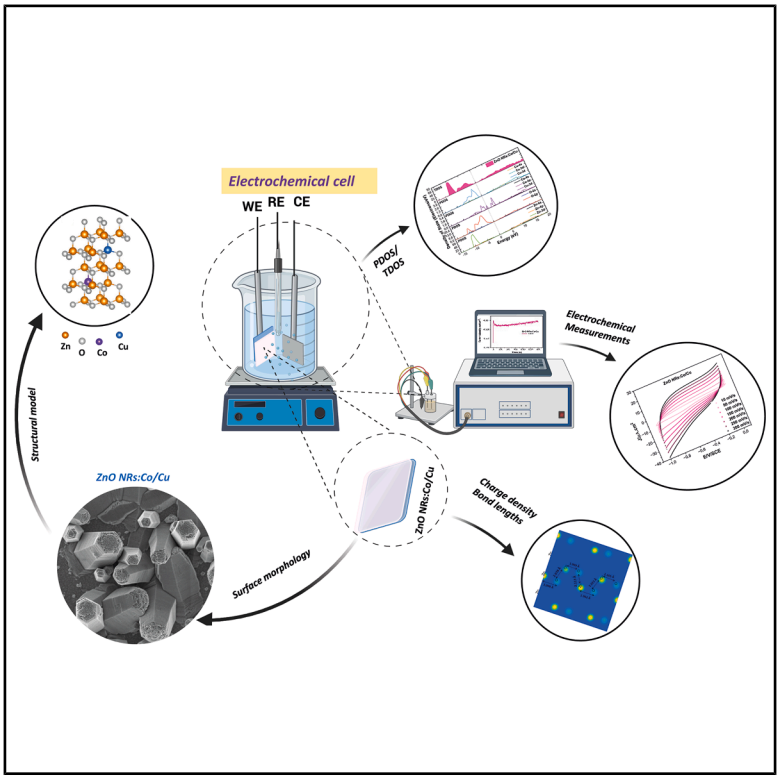

Highlights

- Electrochemical deposition produces Co-, Cu-, and Co-/Cu-doped ZnO nanorods
- PL quenching reveals defect-assisted non-radiative recombination in doped ZnO NRs
- DFT shows dopant-derived states that narrow the ZnO band gap
- Co-/Cu-co-doped ZnO NRs show the lowest R_{ct} and the highest areal capacitance

Authors

I. Boukhoubza, O. El khouja, M. Achehboune, M.A. Basyooni-M. Kabatas, I. Derkaoui, I. Enculescu, E. Matei

Correspondence

issam.boukhoubza@infim.ro (I.B.), m.kabatas@tudelft.nl (M.A.B.-M.K.), elena.matei@infim.ro (E.M.)

In brief

Boukhoubza et al. synthesize Co-/Cu-co-doped ZnO nanorods by electrochemical deposition and show that co-doping modifies the lattice, introduces defect states, and narrows the band gap. The co-doped nanorods exhibit improved charge-transfer kinetics and higher areal capacitance, highlighting the potential of transition-metal co-doping for enhanced ZnO NR-based energy-storage electrodes.

Boukhoubza et al., 2026, Cell Reports Physical Science 7, 103271
May 20, 2026
https://doi.org/10.1016/j.xcrp.2026.103271

CellPress

Cell Reports
Physical Science

CellPress
OPEN ACCESS

Article

Band-gap engineering in Co-/Cu-co-doped ZnO nanorods unlocks superior charge-storage kinetics

I. Boukhoubza,[1,2,*] O. El khouja,[1] M. Achehboune,[3,4] M.A. Basyooni-M. Kabatas,[5,6,7,8,*] I. Derkaoui,[2] I. Enculescu,[1] and E. Matei[1,*]

[1]National Institute of Materials Physics, Atomistilor 405A, 077125 Magurele, Romania
[2]Faculty of Sciences Dhar El Mahraz, University Sidi Mohammed Ben Abdellah, PO Box 1796, Atlas, Fez 30 000, Morocco
[3]School of Applied and Engineering Physics, Mohammed VI Polytechnic University, Ben Guerir 43150, Morocco
[4]Laboratoire de Physique Du Solide, Namur Institute of Structured Matter, University of Namur, Rue de Bruxelles 61, 5000 Namur, Belgium
[5]Department of Precision and Microsystems Engineering, Delft University of Technology, Mekelweg 2, Delft 2628 CD, the Netherlands
[6]Department of Nanotechnology and Advanced Materials, Graduate School of Applied and Natural Science, Selçuk University, Konya 42030, Turkey
[7]Institute of Nanotechnology, Karlsruhe Institute of Technology, Kaiserstraße 12, 76131 Karlsruhe, Germany
[8]Lead contact
*Correspondence: issam.boukhoubza@infim.ro (I.B.), m.kabatas@tudelft.nl (M.A.B.-M.K.), elena.matei@infim.ro (E.M.)
https://doi.org/10.1016/j.xcrp.2026.103271

SUMMARY

Co-/Cu-co-doped ZnO nanorods are synthesized by electrochemical deposition to investigate the effect of co-doping on their structural, optical, electronic, and electrochemical properties. XRD, Raman, SEM, and photoluminescence analyses reveal that Co/Cu incorporation modifies the ZnO lattice, increases defect-related states, and reduces the band gap from 3.11 to 2.15 eV. Density functional theory calculations further show that Co 3d and Cu 3d states appear near the Fermi level and contribute to the observed band-gap narrowing. Electrochemical measurements indicate that the co-doped nanorods exhibit the lowest charge-transfer resistance and the highest areal capacitance among the samples studied. Together, these results show that Co/Cu co-doping improves charge-transfer kinetics in ZnO nanorods and highlights co-doping as an effective strategy for tuning oxide electrodes for energy-storage applications.

INTRODUCTION

Developing advanced energy storage systems has become a strategic research priority in response to escalating global energy demands and the urgent need for sustainable technologies.[1–3] Among existing technologies, electrochemical supercapacitors have emerged as leading candidates due to their unique ability to bridge the gap between batteries and conventional capacitors, offering high power density, rapid charge-discharge capability, excellent reliability, and long operational lifetimes. These attributes make supercapacitors particularly attractive for next-generation applications in portable electronics, electric mobility, aerospace, and biomedical devices.[4,5] Based on their charge storage mechanisms, supercapacitors are classified into electrochemical double-layer capacitors (EDLCs), pseudocapacitors (PCs), and hybrid supercapacitors.[6] EDLCs store energy through non-faradaic electrostatic adsorption of ions at the electrode/electrolyte interface, typically employing high-surface-area carbon-based materials, and are characterized by outstanding cycling stability.[7] In contrast, PCs rely on fast and reversible faradaic redox reactions, often involving transition metal oxides (TMOs) or conductive polymers, which contribute to significantly higher specific capacitance.[8] Hybrid supercapacitors integrate EDLC and PC charge storage mechanisms, offering a synergistic approach to improve overall energy and power density while maintaining excellent cycling performance.[9]

Developing advanced electrode materials with superior electrochemical performance has become a central focus in the pursuit of next-generation supercapacitor technologies.[10] Among the various candidates, nanostructured TMOs have garnered significant attention due to their earth-abundant nature, low cost, environmental compatibility, and rich redox chemistry. Materials such as MnO_2, NiO, CuO, RuO_2, Co_3O_4, and V_2O_5 have demonstrated promising electrochemical properties, making them attractive for energy storage applications.[11–16] ZnO nanostructures have emerged as particularly compelling, combining environmental benignity with high electrical conductivity, notable optical properties, and robust redox activity. ZnO also benefits from a wide direct band gap (3.37 eV), a high surface-to-volume ratio, and excellent cycling stability features, demonstrating its potential as a sustainable and efficient electrode material for high-performance supercapacitors.[6,17]

Doping ZnO nanostructures with transition metal ions is a well-established strategy for tailoring and enhancing their physical and chemical properties. Synthesis techniques, including co-precipitation,[18] hydrothermal,[19] electrochemical deposition,[20]

Please cite this article in press as: Boukhoubza et al., Band-gap engineering in Co-/Cu-co-doped ZnO nanorods unlocks superior charge-storage kinetics, Cell Reports Physical Science (2026), https://doi.org/10.1016/j.xcrp.2026.103271

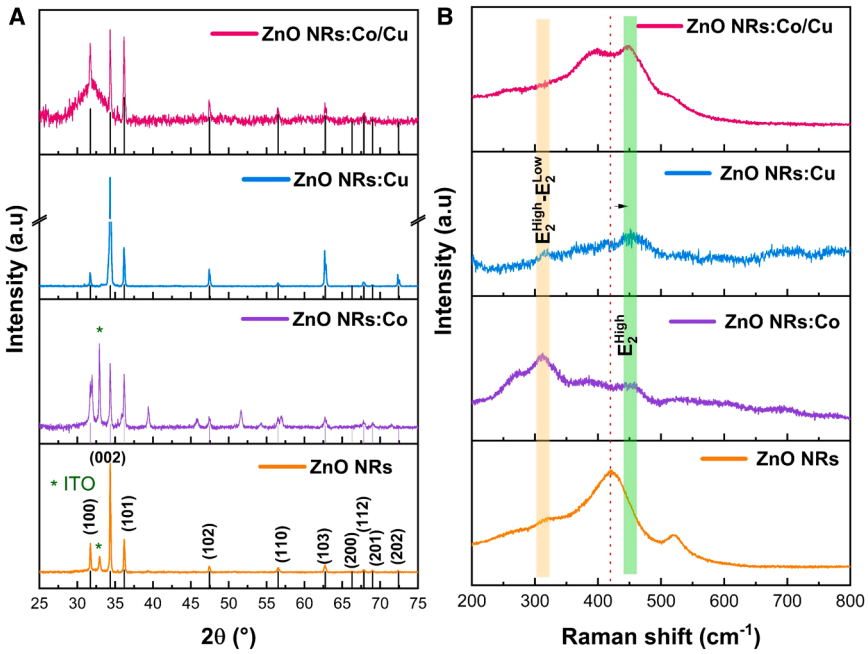

Figure 1. Structural and vibrational characterization

(A) X-ray diffraction (XRD) patterns and (B) Raman spectra of ZnO NRs, ZnO NRs:Co, ZnO NRs:Cu, and ZnO NRs:Co/Cu.

sol-gel,[21] wet chemical approaches[22] have been employed to incorporate dopants into the ZnO lattice. Transition metals such as Co, Cu, Ni, Mn, and Fe are commonly used due to their pronounced influence on the electrical conductivity, optical absorption, magnetic properties, and electrochemical capacitance of ZnO. In this context, Sahu et al.[23] demonstrated that Cd- and Co-co-doped ZnO nanoparticles, synthesized via a sol-gel route, exhibited high specific capacitance and excellent cycling stability, confirming their potential for supercapacitor applications. Chakraborty et al.[24] reported that Al- and Cu-co-doped ZnO NRs, synthesized hydrothermally, showed increased band gap and crystallite size for Al doping, along with a significant enhancement in current density from 0.77 to 4.98 mA/cm^2 and a 1.8-fold improvement in electrochemical response compared to undoped ZnO. Bozzini et al.[25] highlighted the electrodeposition of Mn/Cu-doped ZnO with a biphasic structure, where pulse-plating enabled a stable, self-organized morphochemical distribution that improved hybrid supercapacitor performance. Similarly, Ammar et al.[26] demonstrated that Mn/Cu-doped ZnO nanowires integrated with MXene nanosheets yielded a specific capacitance of 151 F/g and an energy density of 84 Wh/kg, indicating the promise of such hybrid electrodes.

Co-, Cu-, and Co-/Cu-co-doped ZnO NRs are synthesized by electrochemical deposition to examine how transition-metal doping modifies the structure, defect-related states, electronic structure, and electrochemical response of ZnO NRs. Structural and optical analyses show that co-doping changes the local lattice environment, promotes defect-related states, and narrows the band gap. Density functional theory (DFT) calculations support these observations by showing dopant-derived states near the Fermi level. Electrochemical measurements further show that the Co-/Cu-co-doped ZnO NRs exhibit the lowest charge-transfer resistance and the highest areal capacitance among the studied electrodes, highlighting the role of co-doping in improving charge-transfer kinetics in ZnO-based energy-storage materials.

RESULTS AND DISCUSSION

XRD and Raman analysis

Figure 1A illustrates XRD patterns for ZnO NRs, ZnO NRs:Co, ZnO NRs:Cu, and ZnO NRs:Co/Cu prepared by electrochemical deposition. For all samples, the characteristic diffraction peaks situated at 31.91°, 34.59°, 36.42°, 47.77°, 56.86°, 63.19°, 66.70°, 68.29°, and 69.43° can be perfectly assigned to the (100), (002), (101), (102), (110), (103), (200), (112), and (201) lattice planes of the wurtzite hexagonal structure of ZnO, which is following the standard JCPDS data card (JCPDS Card no. 01-075-1526) and has space group P63mc with lattice parameters a = 3.245 Å and c = 5.207 Å, respectively. For ZnO NRs:Co, additional characteristic peaks at 31.3°, 36.6°, 44.8°, and 55.8° can be indexed to the (311), (400), (511), and (111) planes, respectively, corresponding to the phase composition of Co_3O_4/CoO.[27,28] Furthermore, additional peaks in the XRD pattern of ZnO NRs:Cu can be observed at 30.92°, which is attributed to the presence of CuO.[29] Moreover, a high-intensity (002) XRD peak was observed for all samples, indicating a high degree of crystallinity in the prepared ZnO NRs and demonstrating that the nanowires have a preferred c-axis orientation.

The average crystallite size and texture coefficient (TC) of the ZnO nanowires were determined based on the full-width-at-half-maximum (FWHM) and intensities of the (101), (002), and (100) characteristic peaks (Table 1), using the Debye-Scherrer and TC(hkl) formulas, as presented in Equations 1 and 2, respectively.

Please cite this article in press as: Boukhoubza et al., Band-gap engineering in Co-/Cu-co-doped ZnO nanorods unlocks superior charge-storage kinetics, Cell Reports Physical Science (2026), https://doi.org/10.1016/j.xcrp.2026.103271

Table 1. 2θ, FHWM, average crystallite size, and texture coefficient of ZnO NRs, ZnO NRs, ZnO NRs:Co, ZnO NRs:Cu, and ZnO NRs:Co/Cu

Materials	(hkl) Peak	2θ (degree)	FHWM (rad)	Crystallite size nm	Average crystallite size D (nm)	TC
ZnO NRs	**(100)**	31.75	0.185	44.83	47.67	0.51
	(002)	34.35	0.162	51.52	–	1.89
	(101)	36.19	0.180	46.67	–	0.59
ZnO NRs:Co	**(100)**	31.70	0.221	37.52	41.74	0.88
	(002)	34.33	0.178	46.75	–	1.17
	(101)	36.18	0.205	40.96	–	0.96
ZnO NRs:Cu	**(100)**	31.68	0.151	55.04	53.90	0.01
	(002)	34.32	0.142	59.25	–	2.54
	(101)	36.16	0.177	47.41	–	0.24
ZnO NRs:Co/Cu	**(100)**	31.68	0.278	30.06	38.36	0.95
	(002)	34.32	0.213	47.03	–	1.05
	(101)	36.15	0.178	37.99	–	0.94

$$D = \frac{k\lambda}{\beta \cos\theta}, \qquad \text{(Equation 1)}$$

$$TC(hkl) = \frac{I(hkl)/I_0(hkl)}{\frac{1}{N}\sum_{1}^{N} I(hkl)/I_0(hkl)}, \qquad \text{(Equation 2)}$$

Where $k = 0.9$ is a dimensionless shape factor, λ (nm) is the wavelength of CuKα radiation (1.5418 Å), θ represents the Bragg angle, and β corresponds to the FWHM of the diffraction peak. In addition, $I(hkl)$ is the measured intensity, $I_0(hkl)$ refers to the standard intensity from (JCPDS no. 36-1451), and n is the number of reflections ($N = 3$). As shown in Table 1, the higher TC of (002) planes in all samples suggests that the ZnO nanorods preferentially develop along the c-axis orientation.

The vibrational properties of undoped ZnO NRs, as well as the ZnO NRs doped with Co, Cu, and Co/Cu, were studied using Raman spectroscopy upon excitation at 633 nm wavelength, as shown in Figure 1B. The Raman spectrum of ZnO nanorods revealed two distinct peaks at 317 and 422 cm^{-1}. These peaks correspond to the multiphonon scattering mode E_{2H} (High)-E_{2L} (Low) and the non-optical phonon mode E_{2H}, respectively, indicating the formation of the hexagonal wurtzite structure of ZnO.[30] The Raman spectra of ZnO NRs:Co, ZnO NRs:Cu, and ZnO NRs:Co/Cu exhibit similar characteristic peaks, with the E_{2H} mode wavenumber increasing from 423 to 432 cm^{-1}. The shift in the E_2H mode position is mainly attributed to lattice strain and local distortion arising from the substitution of Zn^{2+} ions by Co^{2+} and Cu^{2+} ions, which modifies bond lengths and force constants within the ZnO lattice.[31] The presence of the E_{2H} vibrational mode confirms that the ZnO samples prepared by electrochemical deposition are of high crystalline quality, consistent with the XRD results. In addition, for Co/Cu-doped ZnO NRs, an additional peak at 530 cm^{-1} was observed, which is associated with the quasi-longitudinal optical (LO) phonon mode attributed to dopants coupled with donor defects, particularly doubly occupied oxygen vacancies (V_O), while zinc interstitials (Zn_i) and dopant-defect complexes may also contribute to its activation.[32,33] According to previous reports, the enhanced intensity of this mode in the co-doped sample suggests an increased defect density induced by simultaneous Co and Cu incorporation rather than the presence of a single dominant defect species.[31]

SEM and EDX analysis

Figure 2 shows SEM images and diameter-size distribution histograms of the Co-, Cu-, and Co-/Cu-doped ZnO nanorods during the electrochemical process. Pure ZnO NRs clearly show the formation of a hexagonal structure's growth along the c-axis and planar face at their top, with an average diameter of around 235 nm (Figures 2A and 2E). Figures 2B–2D exhibit that the morphological characteristics changed after doping. For the Cu-doped ZnO NRs, Figure 2G shows the formation of nanorods with a decrease in length and diameter (around 172 nm), and the nanorods are more aggregated and irregular, most likely due to increased interaction with the ZnO lattice, which interferes with preferred growth. Furthermore, Figures 2F and 2H show the formation of nanorods with average diameters of approximately 217 and 184 nm, respectively. In addition, Co doping induces remarkable changes, particularly on the nanorods' top surfaces, resulting in a rougher, more faceted structure. This may indicate preferential Co incorporation at these sites, perhaps changing the termination of crystal planes.

The compositional uniformity of Co- and Cu-doped and co-doped ZnO nanorods on ITO substrates was examined using energy-dispersive X-ray mapping, as shown in Figure S1. The images show the areas where the elemental mapping for zinc, oxygen, cobalt, and copper was performed. The results agree with the expected chemical composition, confirming that Co-/Cu-co-doped ZnO NRs were successfully fabricated.

Optical and electronic structures

Figure 3 shows PL spectroscopy results used to better understand the intrinsic and extrinsic defects in ZnO NRs and doped ZnO NRs. As shown in the PL spectra of all samples, five distinct emission bands are observed at 382 nm (UV emission), 410 nm (light violet emission), 432 nm (violet emission), 465 nm (blue

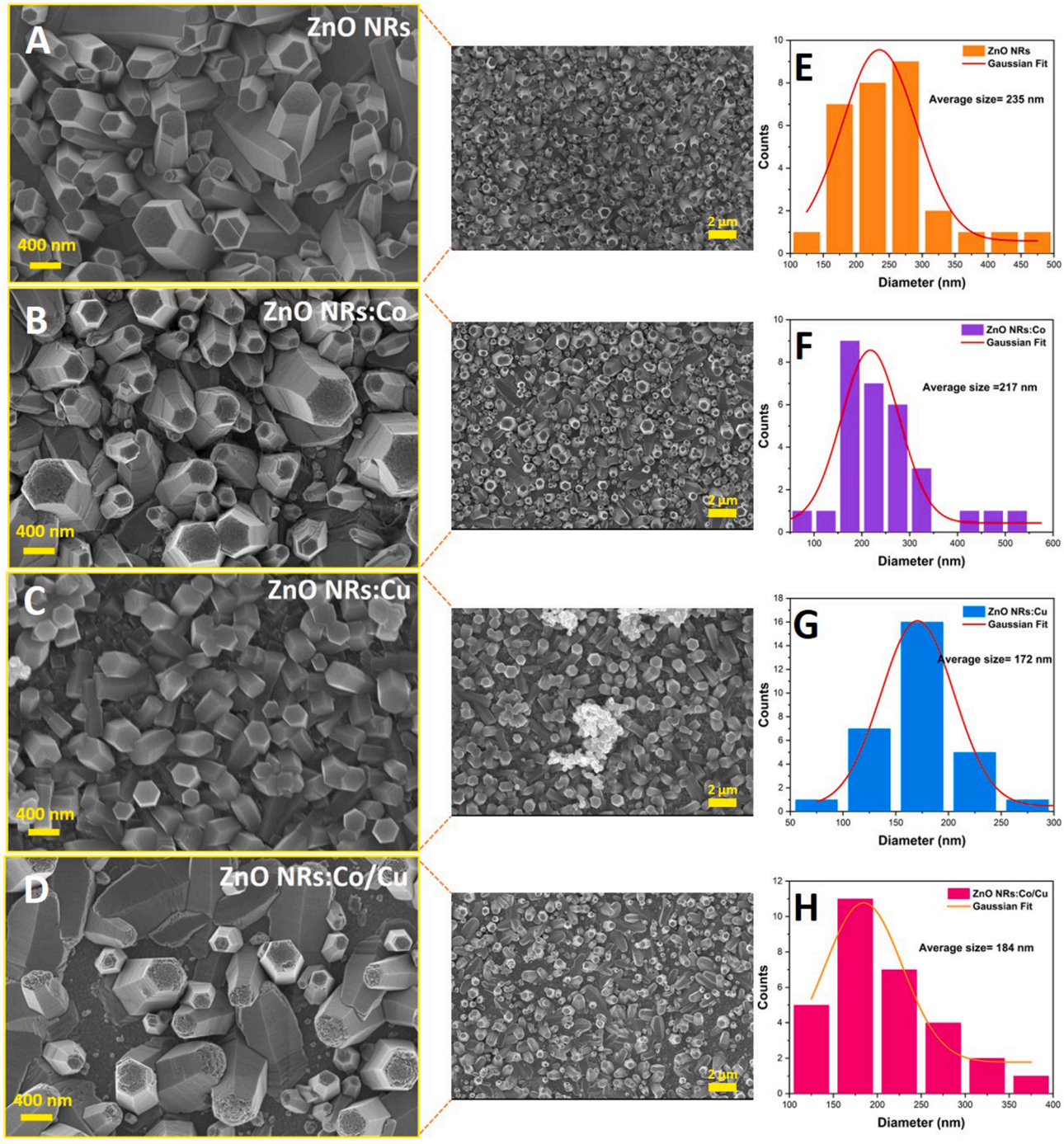

Figure 2. Morphology characterization and average diameter of ZnO NRs

(A–D) SEM images of ZnO NRs (A), ZnO NRs:Co (B), ZnO NRs:Cu (C), and ZnO NRs:Co/Cu (D).

(E–H) Diameter size-distribution histograms of ZnO NRs (E), ZnO NRs:Co (F), ZnO NRs:Cu (G), and ZnO NRs:Co/Cu (H).

emission), and a sharp band centered at 561 nm (green emission). Compared to undoped ZnO, the PL emission intensity is quenched in doped and co-doped ZnO NRs. This reflects a decrease in defect-related recombination processes. The incorporation of Co^{2+} and Cu^{2+} ions introduces non-radiative recombination pathways and charge transfer processes, which lead to PL quenching and a reduction in defect states in the doped ZnO NRs.[34,35]

To understand the origin of the emission bands, the PL spectra in the 350–650 nm range were fitted using Gaussian analysis. The emission band observed at 382 nm is attributed to excitonic recombination, which corresponds to the near-band-edge (NBE)

Please cite this article in press as: Boukhoubza et al., Band-gap engineering in Co-/Cu-co-doped ZnO nanorods unlocks superior charge-storage kinetics, Cell Reports Physical Science (2026), https://doi.org/10.1016/j.xcrp.2026.103271

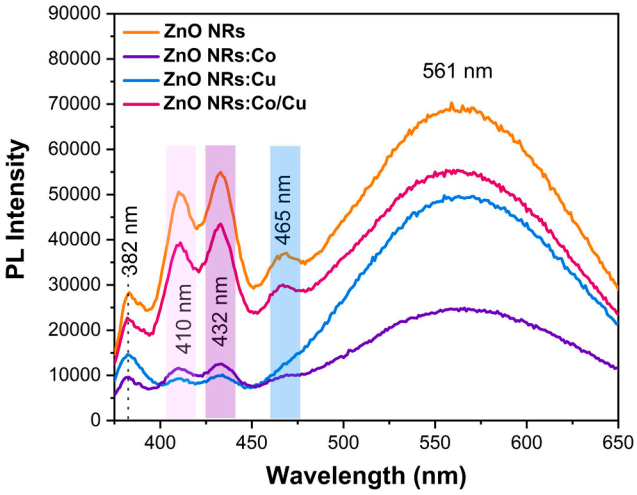

Figure 3. Photoluminescence characterization: photoluminescence (PL) spectra of ZnO NRs, ZnO NRs:Co, ZnO NRs:Cu, and ZnO NRs:Co/Cu

emission of wide-band-gap ZnO.[36] The violet emission bands appearing at 410 nm (3.02 eV) and 432 nm (2.87 eV) are associated with electron transitions from zinc interstitials with different charge states, such as neutral (Zn_i), singly charged (Zn_i'), and doubly charged (Zn_i''), to the valence band (VB), respectively.[37,38] The blue emission band located in the 465 nm (2.66 eV) range can be attributed to V_{Zn}. Therefore, a strong emission band ranging from 500 to 650 nm can be deconvoluted into four Gaussian fits (see Figure S2), including green (533 nm [2.32 eV] and 561 nm [2.21 eV]), yellow (around 598 nm), and red (around 648 nm) emissions. These visible emissions are attributed to oxygen-related defects in ZnO, primarily oxygen vacancies (V_O) in their neutral and ionized states, as well as oxygen interstitials. Green emission is commonly associated with singly ionised oxygen vacancies (V_o^+), yellow emission originates from doubly ionised vacancies (V_o^{++}), and red emission is associated with oxygen interstitial (O_i) defects.[37,39]

Figures 4A–4D displays a Tauc plot for undoped and doped ZnO NRs to illustrate the shift in ZnO's band gap energy. The band gap values were calculated using the Tauc equation[40]:

$$\alpha h\nu = (h\nu - Eg)^{1/2} \quad \text{(Equation 3)}$$

Where α is the absorption coefficient, $h\nu$ is the photon energy, and E_g is the band gap energy.

As shown in Figures 4A–4E, ZnO NRs exhibit a band gap energy of 3.11 eV, which agrees with the values reported in our previous work.[41] For doped ZnO NRs, the band gap energy decreased; this behavior is associated with the creation of intragap states, which lower the ZnO Fermi level. The band gap energy of Co-doped ZnO NRs (Figures 6B–6F) was shifted to 2.77 eV, which can be induced by s-d and p-d exchange interactions between ZnO and Co^{2+} ions.[42] As illustrated in this figure, the presence of Co^{2+} 3d levels inside the ZnO band gap facilitates the formation of new energy bands at longer wavelengths.[43] Meanwhile, the band gap modification in the case of Cu-doped ZnO NRs (Figures 4C–4G) can be attributed to the intergap transition between the 3d states of Cu and the 4s states of ZnO.[44] Furthermore, the Co-/Cu-co-doped ZnO NRs show the lowest band gap compared to the other samples (Figures 4D–4H).

To further understand the electronic characteristics of doped ZnO and how distinct atomic orbitals contribute to each energy band, we calculated the total and partial densities of states, as shown in Figures 4I–4L. As seen in Figure 4A, the valence band (VB) of ZnO can be separated into three regions: the upper VB, from −5.42 to 0.03 eV; the middle VB, from −8.8 to −5.4 eV; and the lower VB, from 15.5 to −13.8 eV. The portion from the Fermi level to −5.42 eV is primarily derived from the O 2p and 2s orbitals. The middle part of the VB is composed of Zn 3d orbitals with a small contribution from O 2p states. The lower part of the VB originates primarily from the O 2s orbitals, with a partial contribution from the Zn 3d states. Moreover, the lowest conduction band (CB) is influenced mainly by Zn 4s states, with partial mixing from Zn 4p and O 2p states.

When Zn atoms are substituted by Co or Cu atoms, the Fermi level shifts upward into the conduction band, showing that electrons start occupying its lowest energy states. Figures 4J and 4K show the PDOS for Co-doped ZnO NRs and Cu-doped ZnO NRs. For Co- and Cu-doped ZnO, the Co 3d and Cu 3d states contribute to the CB and VB, respectively (Figures 4F and 4G). In the case of co-doped ZnO, incorporating Co atoms exerts a more pronounced effect on both the conduction band and the valence band, with the appearance of Co-3d states acting as localized impurity levels, whereas the Cu-3d states are more deeply integrated into the valence band, hybridizing strongly with the O-2p states and shifting the valence band maximum (VBM) closer to E_F with a minor influence on the conduction band. PDOS analysis shows that the electronic states near the Fermi level are primarily derived from the p and d orbitals of Co and Cu. In addition, compared to the upper VB formed by the Zn 3d states, the upper VB associated with the Co 3d or Cu 3d states shifts to higher energies, where certain energy levels extend above the Fermi level. In the co-doped system, a synergistic effect is observed. There is a simultaneous contribution of both Co-3d and Cu-3d orbitals near E_F. This collective hybridization creates a higher density of states at the VBM compared to the mono-doped systems. This orbital overlap between the two dopants and the oxygen host facilitates narrower energy transitions, which correlate with the experimental (redshift/conductivity) observed in the ZnO NWs: Co/Cu samples. Notably, the DOS of Cu in co-doped ZnO is reduced compared to that of Co or Cu in singly doped ZnO. These observations indicate a transfer of electrons from Cu to Co atoms when both are introduced into the ZnO lattice, leading to an enhancement in the DOS of Co atoms and a reduction in the DOS of Cu atoms above the Fermi level.

To evaluate the physical properties of doped ZnO NRs, it is crucial to examine their structural, thermodynamic, and dynamical stability. Structural stability is closely tied to the bonding nature and atomic arrangement, which can be effectively visualized through charge density plots. Figure 5 presents the charge density distributions and bond lengths for (a) pure ZnO NRs, (b) ZnO NRs:Co, (c) ZnO NRs:Cu, and (d) ZnO NRs:Co/Cu. In undoped ZnO NRs (Figure 5A), the Zn-O bond lengths are uniform at

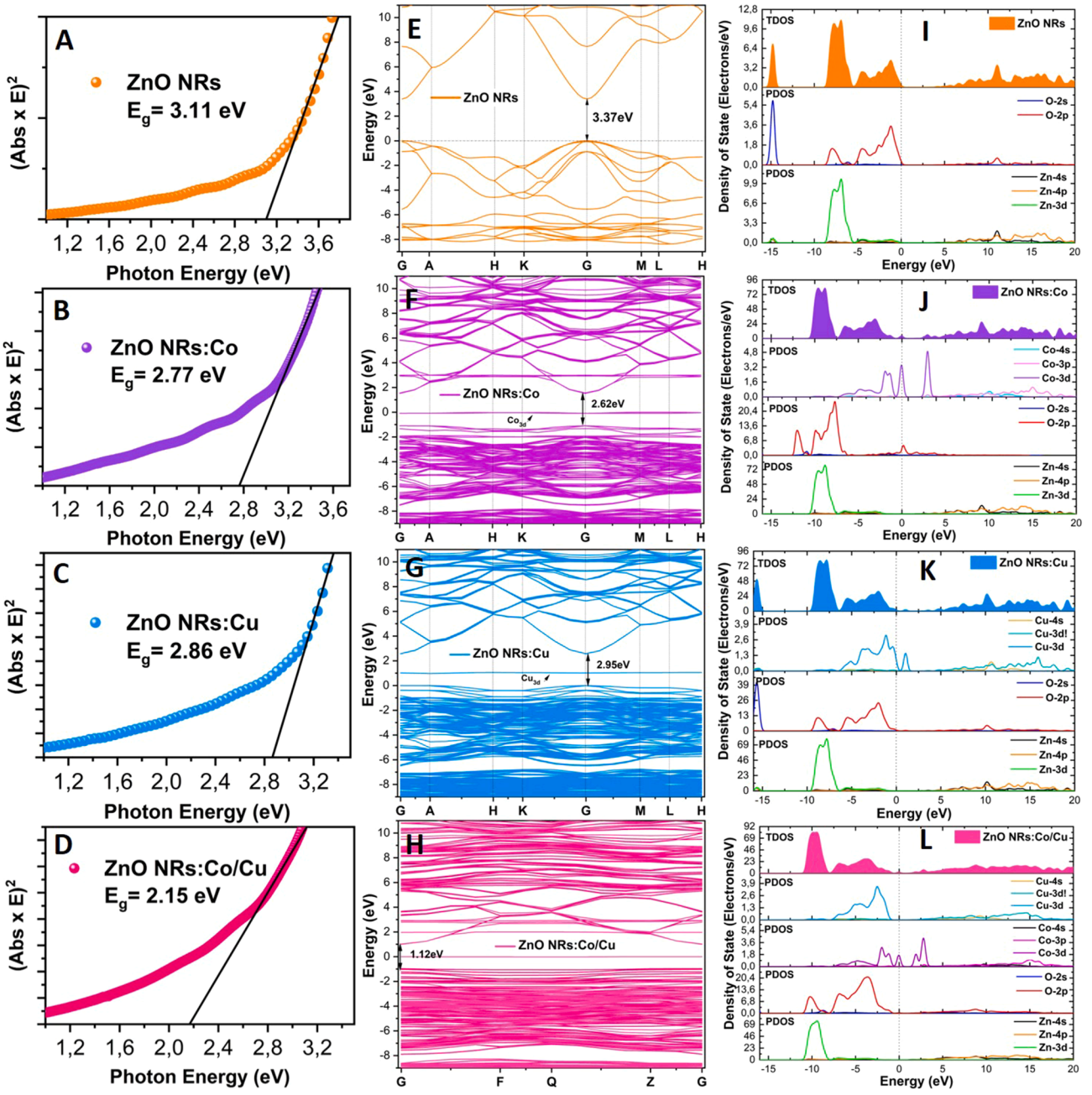

Figure 4. Band gap energy and electronic structure

(A–D) Tauc plots used to estimate the optical band gap of ZnO NRs (A), ZnO NRs:Co (B), ZnO NRs:Cu (C), and ZnO NRs:Co/Cu (D).

(E–H) Electronic band structures calculation of ZnO NRs (E), ZnO NRs:Co (F), ZnO NRs:Cu (G), and ZnO NRs:Co/Cu (H).

(I–L) Total and partial density of states (TDOS/PDOS) for ZnO NRs (I), ZnO NRs:Co (J), ZnO NRs:Cu (K), and ZnO NRs:Co/Cu (L), with the Fermi level set at 0 eV.

approximately 1.976–1.987 Å, reflecting the wurtzite structure's inherent symmetry and bonding environment. Upon doping with Co (Figure 5B), notable changes occur in the local charge density and bond lengths. The Co-O bonds range from 2.002 Å to 2.017 Å, which is longer than the original Zn-O bonds, indicating local structural distortion and altered electronic interactions. Similarly, in Cu-doped ZnO (Figure 5C), the Cu-O bond lengths vary from 1.913 Å to 1.997 Å, again indicating disruption of the original ZnO bonding environment. The asymmetry in bond lengths suggests localized strain and a redistribution of charge density due to the presence of Cu, which has a different electronegativity and ionic radius than Zn. In the case of Co/Cu co-doping (Figure 5D), even more significant modifications in bond lengths and charge distribution are observed. Co-O and

Please cite this article in press as: Boukhoubza et al., Band-gap engineering in Co-/Cu-co-doped ZnO nanorods unlocks superior charge-storage kinetics, Cell Reports Physical Science (2026), https://doi.org/10.1016/j.xcrp.2026.103271

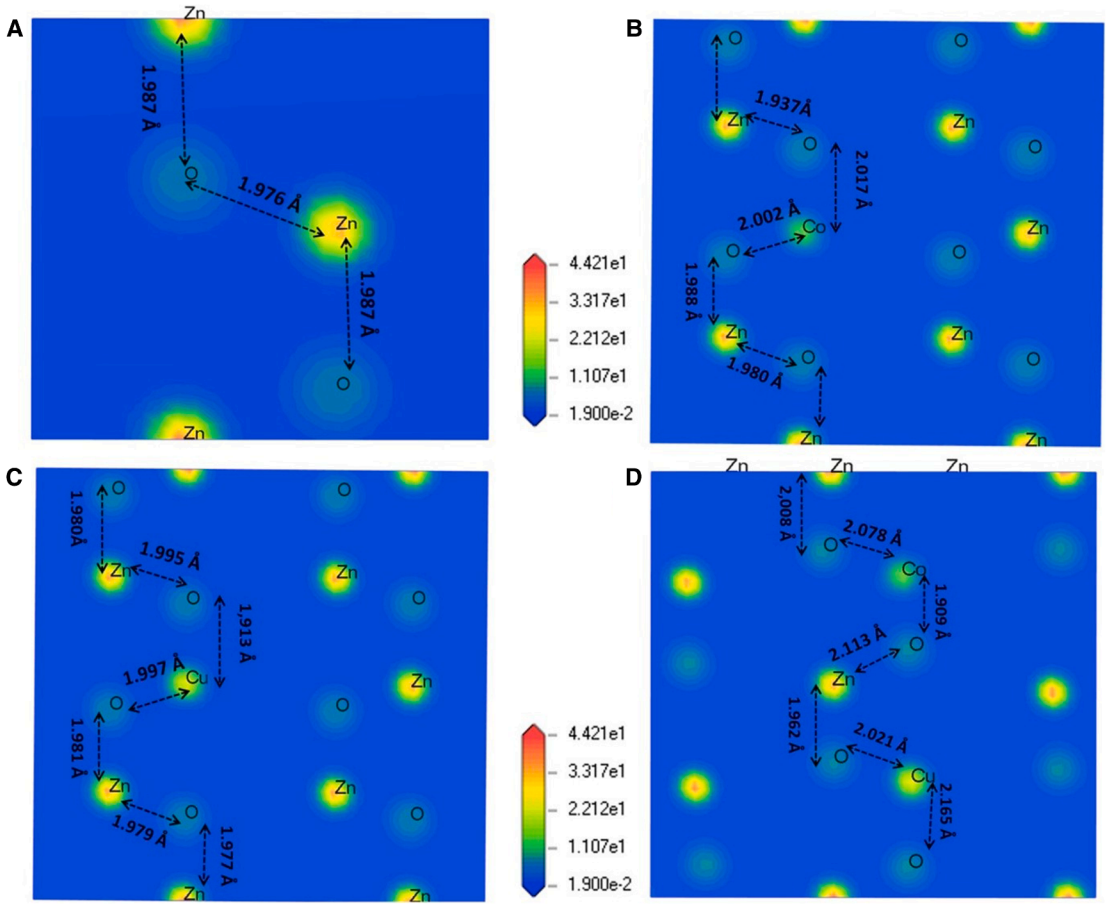

Figure 5. Charge density distribution of undoped and doped ZnO NRs

(A–D) Charge density distribution maps of ZnO NRs (A), ZnO NRs:Co (B), ZnO NRs:Cu (C), and ZnO NRs:Co/Cu (D) along the (110) orientation. The color scale represents the electron density, with red and yellow regions indicating higher density. Bond lengths (in Å) are labeled to highlight variations in the local bonding environment induced by doping.

Cu-O bonds extend up to 2.078 Å and 2.009 Å, respectively, while adjacent Zn-O bonds stretch to 2.113 Å. These changes imply a combined influence of both dopants on the ZnO lattice, potentially enhancing defect formation, modifying electronic structure, and enabling synergistic effects. Overall, doping ZnO NRs with Co, Cu, or both alters the local bonding structure, as evidenced by the variations in bond lengths and charge densities. These structural modifications indicate the formation of new chemical environments, which could significantly influence the material's electronic, optical, and magnetic properties. Understanding these effects is vital for optimizing doped ZnO nanostructures for targeted applications in optoelectronics, photocatalysis, and spintronics.

Dielectric, reflectivity, refractive index, and absorption coefficient

For more details on the electronic transitions, Figure 6A illustrates the imaginary part $\varepsilon_2(\omega)$ of undoped and doped ZnO NRs. For ZnO NRs, three dominant peaks appear at around 3.2–4.5 eV, 6.5–10 eV, and 15.53 eV. The peak observed at approximately 3.2–4.5 eV corresponds to electronic transitions from the O 2p states in the VB to the Zn 4s states in the CB, occurring near the band gap energy (3.37 eV). The second and third peaks, at around 6.50 eV and 13.02 eV, are attributed to transitions from VB (Zn 3d) to VB (O 2p) and from VB (Zn 3d) to CB (O 2s), respectively. These transitions are consistent with the DOS analysis shown in Figure 4I. In the case of Co- and Cu-doped ZnO NRs, the first and second peaks are redshifted, while the third peak exhibits a small blueshift. Furthermore, the intensity of the first of the two peaks is more intense in the ZnO NRs:Co/Cu than in the doped ZnO NRs. This suggests a higher probability of electronic transitions from the O 2p states at the top of the valence band to the Zn 4s states at the bottom of the conduction band, driven by concurrent Co and Cu co-doping.

Figures 6B–6D show the reflectivity, refractive index, and absorption of ZnO NRs and Co- and Cu-doped and co-doped ZnO NRs, respectively. The reflectivity most closely indicates its dominance in the ultraviolet (UV) region, since it has a small peak at about 16.48 eV. Unlike pure ZnO NRs, the reflectivity of the co-doped samples increases over the 0–25 eV range and shifts into the visible range. The refractive index also exhibits

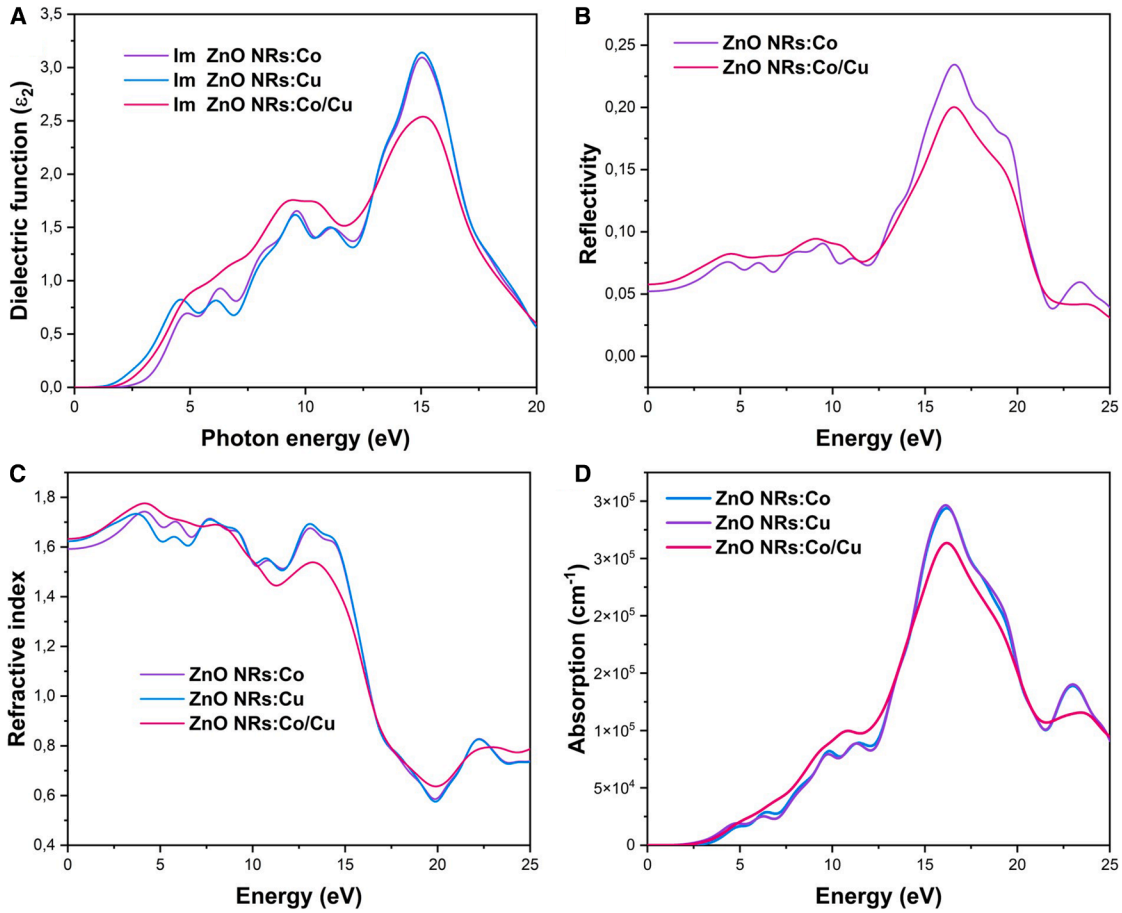

Figure 6. Optical properties of undoped and doped ZnO NRs

(A–D) Calculated imaginary part of the dielectric function (A), reflectivity (B), refractive index (C), and absorption spectra (D) of ZnO NRs, ZnO NRs:Co, ZnO NRs:Cu, and ZnO NRs:Co/Cu.

a sharp increase in the low-energy regime and is strongly affected by doping, particularly in co-doped ZnO NRs. The initial refractive indices of undoped, Co-doped, Cu-doped, and Co/Cu-co-doped ZnO NRs are approximately 1.580, 1.589, 1.618, and 1.635, respectively. This increase in the refractive index at low energies, as seen, indicates a reduction in the band gap due to Co and/or Cu doping. In addition, as shown in Figure 6D, the absorption band is observed in the UV range and is relatively broad. Co- and Cu-atom doping shifts the absorption peaks toward higher energy. This could be attributed to an increase in the carrier concentration.

Electrochemical properties

Figures 7A–7D presents the cyclic voltammetry profiles of ZnO-based electrodes, namely ZnO NRs, ZnO NRs:Cu, ZnO NRs:Co, and ZnO NRs:Co/Cu, recorded at scan rates ranging from 10 to 300 mV s^{-1}. These profiles reveal substantial enhancements in electrochemical performance upon metal modification. The pristine ZnO exhibits quasi-rectangular CV curves with a relatively low current response, indicating its poor intrinsic electrical conductivity and limited redox activity. Upon Cu incorporation, a significant increase in current density was observed, particularly in the cathodic region. The curves showed pronounced slope asymmetry, reflecting enhanced electron transfer kinetics likely due to the introduction of Cu, which acts as an electronic bridge, facilitating charge-carrier mobility.

In contrast, ZnO NRs:Co electrodes exhibit broader and more defined redox peaks, characteristic of Co^{2+}/Co^{3+} transitions, suggesting faradaic pseudocapacitive contributions. The ZnO NRs:Co/Cu electrode demonstrates superior performance compared to all other compositions, exhibiting the most distinct redox features and the highest current response across all scan rates, underscoring a synergistic effect between Cu and Co dopants that boosts both electronic conductivity and the density of electrochemically active sites. To provide further context for these results, it is helpful to compare the electrochemical behavior of the ZnO NRs:Co/Cu electrode with that of previously reported transition-metal-doped ZnO systems. Single-dopant ZnO electrodes, such as those doped with Nd, Ni, or Ag, have been shown to enhance charge storage primarily through defect generation and moderate improvements in electrical conductivity. For example, Nd-doped ZnO showed a significant increase in capacitance compared to pristine ZnO due to increased defect density and charge-transfer capability.[23] Meanwhile, Ni-doped

Please cite this article in press as: Boukhoubza et al., Band-gap engineering in Co-/Cu-co-doped ZnO nanorods unlocks superior charge-storage kinetics, Cell Reports Physical Science (2026), https://doi.org/10.1016/j.xcrp.2026.103271

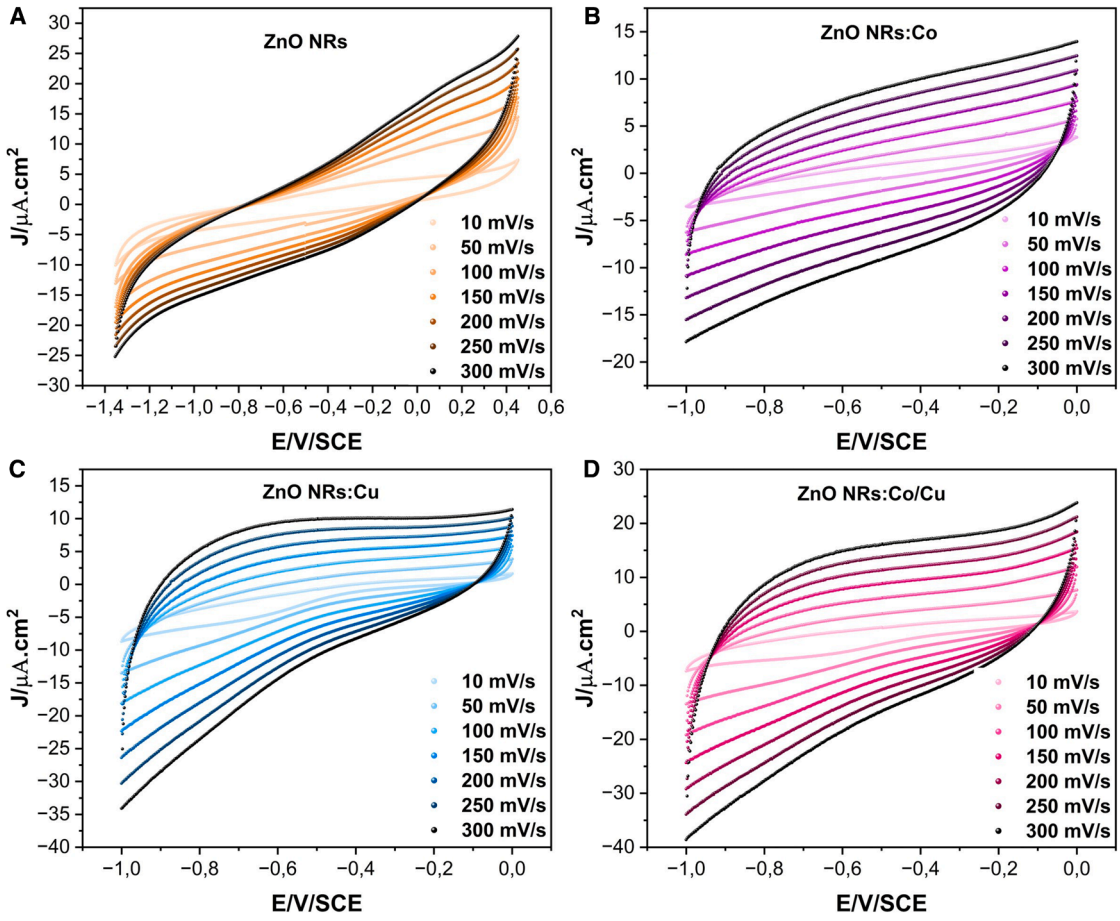

Figure 7. Cyclic voltammetry (CV) measurement of undoped and doped ZnO NRs

(A–D) CV curves of ZnO NRs (A), ZnO NRs:Co (B), ZnO NRs:Cu (C), and ZnO NRs:Co/Cu (D) recorded at scan rates ranging from 10 to 300 mV s^{-1}.

ZnO nanostructures exhibited higher capacitance values due to improved conductivity and an increased electrochemically active surface area.[45] Similarly, Ag-doped ZnO electrodes exhibited reduced interfacial resistance and increased areal capacitance due to improved electron mobility.[46] However, these single-dopant systems generally exhibit limited control over the simultaneous enhancement of conductivity and redox activity. However, the present Co/Cu co-doped ZnO nanorods exhibit lower charge-transfer resistance and higher areal capacitance. This highlights a cooperative dopant effect that optimizes the electronic structure, defect density, and interfacial kinetics, achieving results beyond those typically obtained with individual dopants. Therefore, the superior electrochemical activity of the ZnO NRs:Co/Cu composite is further supported by its reduced charge transfer resistance (R_{ct}), derived from electrochemical impedance spectroscopy (EIS) measurements (see Nyquist plot in Figure 8).

The electronic structure modifications revealed by DFT provide a fundamental explanation for the enhanced electrochemical kinetics observed in our experiments. Specifically, the ZnO NRs:Co/Cu system exhibits a significant increase in the density of states (DOS) near the Fermi level (E_F) due to the hybridization of Co-3d and Cu-3d orbitals (Figure 6H and 6L). This increased electronic density at E_F facilitates a more efficient charge transfer process at the electrode/electrolyte interface. This theoretical finding is directly supported by our EIS measurements, where the ZnO NRs:Co/Cu composite showed a significantly reduced charge transfer resistance (R_{ct}) compared to the mono-doped samples. Essentially, the bridge formed by overlapping dopant orbitals lowers the energy barrier to electron exchange, enabling faster redox kinetics and more efficient ion-electron coupling during charge storage.

The Nyquist plot reveals marked differences in charge transfer and interfacial characteristics of the electrodes (Figure 8A). The semicircular arcs in the high-frequency region reflect the R_{ct} at the electrode/electrolyte interface. At the same time, the linear portion at lower frequencies corresponds to the Warburg impedance, associated with ion diffusion processes. The pristine ZnO exhibits the largest semicircle, indicative of a high R_{ct} (~45 kΩ) and sluggish charge-transfer kinetics, likely due to its limited conductivity and fewer active sites. In contrast, the ZnO NRs:Cu and ZnO NRs:Co composites demonstrate progressively smaller semicircles, with estimated Rct values of ~22 kΩ and ~17 kΩ, respectively. This improvement is attributed to

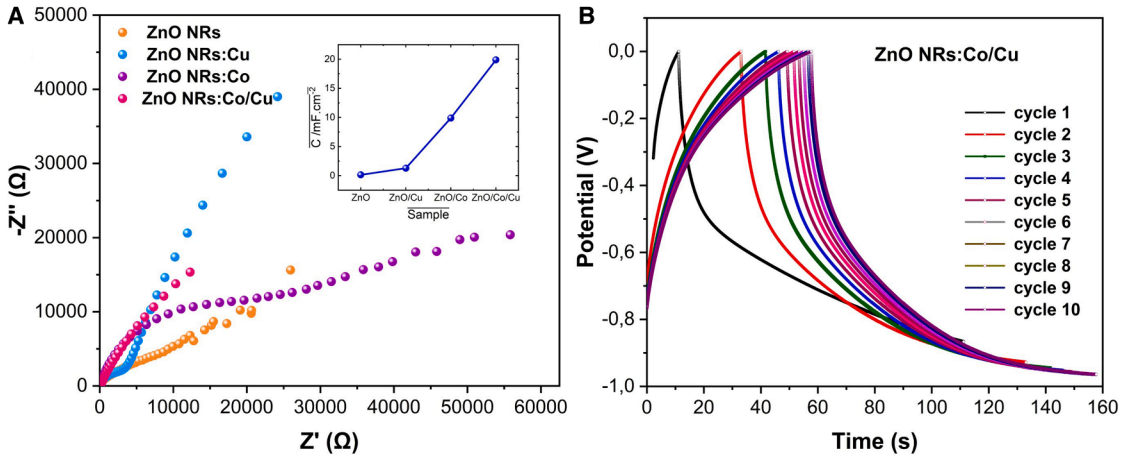

Figure 8. Electrochemical performance of undoped and doped ZnO NRs

(A and B) EIS spectra (A) and GCD profiles (B) of ZnO NRs, ZnO NRs:Co, ZnO NRs:Cu, and ZnO NRs:Co/Cu. The inset in (A) shows the areal capacitance (C) of the electrodes.

the enhanced electrical conductivity and redox activity imparted by Cu and Co dopants. Notably, the ZnO NRs:Co/Cu electrode exhibits the smallest arc, corresponding to an R_{ct} of approximately 6 kΩ. This highlights a synergistic effect between Cu and Co, significantly reducing interfacial resistance and promoting rapid electron transfer.

Additionally, the series resistance (R_s), determined from the interception on the real axis (Z′), decreases in the same trend, with ZnO NRs:Co/Cu showing the lowest Rs (∼380 Ω), compared to ZnO NRs (∼910 Ω). Due to the dual-metal modification, this low series resistance indicates improved bulk conductivity and electrode/electrolyte contact. The inset graph further supports these findings, showing the areal capacitance (C) of the electrodes (Inset Figure 8A). The capacitance increases steadily from ZnO NRs (<1 mF·cm^{-2}) to ZnO NRs:Cu (∼5 mF·cm^{-2}), ZnO NRs:Co (∼12 mF·cm^{-2}), and peaks with ZnO NRs:Co/Cu (∼20 mF·cm^{-2}). This trend confirms that metal doping enhances charge transfer kinetics and increases the density of electrochemically active sites, resulting in superior capacitive behavior. The EIS and capacitance data collectively affirm the improved electrochemical performance of ZnO NRs:Co/Cu, making it a promising candidate for applications in supercapacitors or electrocatalytic systems.

The galvanostatic charge-discharge (GCD) profiles of the ZnO NRs:Co/Cu electrode over ten consecutive cycles, as shown in Figure 8B, provide additional insight into its electrochemical behavior. The measurements were intentionally limited to 10 cycles, which is sufficient to stabilize the electrode/electrolyte interface and to assess the intrinsic charge-storage behavior and electrochemical reversibility of the ZnO nanorod electrodes under the investigated conditions. Each curve shows a nearly symmetrical triangular shape, indicating a reversible charge-discharge process with contributions from both EDLC capacitance and faradaic reactions. The voltage-time profiles remain similar from cycle to cycle, especially after the initial cycles, indicating stable electrochemical behavior and good coulombic efficiency within the 10-cycle measurement window. The slight variation observed in the first cycles likely reflects a short activation process associated with electrolyte penetration and gradual access to additional redox-active sites. This agrees with the CV and EIS results, where ZnO NRs:Co/Cu shows the highest current response, the lowest charge-transfer resistance (Rct ≈6 kΩ), and the lowest series resistance (Rs ≈ 380 Ω). Together, these results confirm that Co/Cu co-doping improves charge transport and interfacial electrochemical behavior in ZnO nanorods.

This study focuses on the intrinsic behavior of the ZnO-based electrodes in a three-electrode configuration and on the materials-level relationship between co-doping, electronic structure, and charge-transfer kinetics. Some limitations should therefore be noted. The GCD analysis is limited to 10 cycles and is used here to evaluate short-term reversibility rather than long-term cycling durability. In addition, full-cell testing is not included in the present work, so practical device-level metrics such as energy density and power density remain to be evaluated. Future studies should therefore extend the cycling analysis over longer durations and examine the performance of Co/Cu co-doped ZnO nanorods in full-cell configurations to further assess their application potential.

In summary, Co, Cu, and Co/Cu doped ZnO nanorods are synthesized by electrochemical deposition, and the effect of doping on their structural, optical, electronic, and electrochemical properties is examined. XRD, Raman, SEM, and PL analyses show that doping modifies the ZnO lattice, changes the local defect structure, and affects carrier recombination behavior. The band gap decreases from 3.11 to 2.15 eV after co-doping, in agreement with the DFT results, which show dopant-derived states near the Fermi level. Electrochemical measurements further show that the Co/Cu co-doped ZnO nanorods exhibit the lowest charge-transfer resistance and the highest areal capacitance among the samples studied. These results show that Co/Cu co-doping is an effective way to tune the electronic structure and improve the electrochemical response of ZnO nanorods for energy-storage applications.

Please cite this article in press as: Boukhoubza et al., Band-gap engineering in Co-/Cu-co-doped ZnO nanorods unlocks superior charge-storage kinetics, Cell Reports Physical Science (2026), https://doi.org/10.1016/j.xcrp.2026.103271

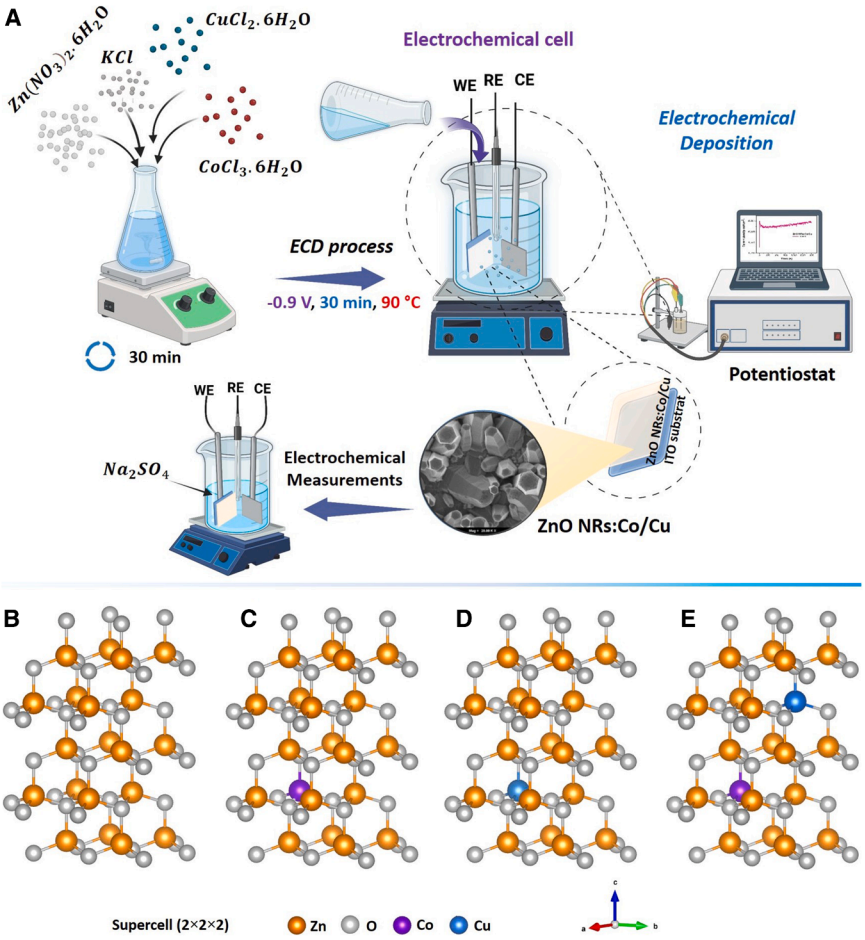

Figure 9. Schematic process and structural models of undoped and doped ZnO NRs

(A) Schematic illustration of the electrochemical deposition of Co/Cu co-doped ZnO NRs.

(B–E) Structural models of undoped ZnO NRs (B), ZnO NRs:Co (C), ZnO NRs:Cu (D), and ZnO NRs:Co/Cu (E).

METHODS

Preparation of Co-/Cu-co-doped ZnO NRs

Co-/Cu-co-doped ZnO nanorods (NRs) were electrodeposited onto ITO substrates using an electrochemical workstation (Metrohm-Autolab: VIONIC powered by INTELLO, Netherlands) in a three-electrode configuration (Figure 9A). The setup consisted of an ITO substrate (1 cm × 2 cm) as the working electrode (WE), Pt foil as the counter electrode (CE), and an Ag/AgCl electrode (in a KCl-saturated aqueous solution) as the reference electrode (RE). To deposit the ZnO nanorods, an electrolyte solution composed of 5 mM Zn $(NO_3)_2{\cdot}6H_2O$ and 100 mM KCl was used. For doped ZnO NRs, three doping concentrations were prepared by adding 0.3125 mM $CuCl_2{\cdot}6H_2O$, 0.3125 mM $CoCl_3{\cdot}6H_2O$, and 0.3125 mM ($CoCl_3{\cdot}6H_2O$/$CuCl_2{\cdot}6H_2O$) to the ZnO solution. The effect of Co, Cu, and the Co/Cu ratio was also examined. Without stirring, the samples were electrodeposited at −0.9 V vs. RE for 30 min at 90°C. After electrodeposition, the as-deposited samples were rinsed with distilled water and dried.

Electrochemical measurements

Metrohm-Autolab: VIONIC powered by INTELLO electrochemical workstation was used to perform electrochemical measurements. The electrochemical cell consisted of a three-electrode system: the Ag/AgCl electrode (in a KCl-saturated aqueous solution) served as the RE, the platinum sheet as the CE, and the ITO electrode as the WE. The electrolyte used was a 1 M Na_2SO_4 aqueous solution. The choice of electrolyte and its concentration was optimized through comparative cyclic voltammetry measurements (Figures S3 and S4). Among the investigated Na_2SO_4 concentrations (0.5–1.5 M), the 1.0 M electrolyte exhibited the highest current response and CV enclosed area, indicating optimal ionic transport and interfacial charge storage. In addition, Na_2SO_4 showed a more favorable electrochemical response than KOH and the Li-based electrolyte, and was therefore selected for all subsequent measurements. CV, GCD, and EIS were performed to investigate the electrochemical performance of the sample electrodes.

Characterization

XRD measurements were used to study the structural properties of undoped and doped ZnO NRs. The analysis was performed using a Bruker D8 X-ray diffractometer with Cu Kα radiation (λ = 0.15406 nm) over the 2θ range of 25°–75°. The morphological characteristics were examined using a Zeiss Gemini 500 FESEM and a Bruker energy-dispersive X-ray (EDX) detector.

The vibrational properties of the samples were determined by Raman spectroscopy (Horiba Jobin-Yvon: Edison) using a He-Ne laser at λ_{exc} = 633 nm. The photoluminescence measurements were carried out at room temperature using an Edinburgh FL 920 PL spectrometer with 325 nm UV excitation. Optical analysis was conducted using a Lambda 45 PerkinElmer UV-Vis spectrophotometer.

DFT calculations

Our theoretical analysis employs spin-polarized DFT within the CASTEP code.[47] The electronic interactions are modeled using the generalized gradient approximation (GGA) with the Perdew-Burke-Ernzerhof (PBE) functional and the Hubbard correction to account for exchange-correlation effects.[48] The ion-electron interaction is described using a projector-augmented wave (PAW) pseudopotential, which ensures an accurate representation of the system's electronic structure. The valence-electron configurations for Zn (s^2d^{10}), O (s^2p^4), Co (d^7s^2), and Cu (d^1s^1) were used in the calculations. A plane-wave cutoff energy of 450 eV was applied to the 2 × 2×2 ZnO supercell structures (Figure 9B), with Brillouin zone sampling conducted using a 4 × 4×5 Γ Monkhorst-Pack grid. For mono-doping (6.25% doping concentration), a Zn atom was substituted with Co in ZnO NRs:Co and with Cu in ZnO NRs:Cu (Figures 9C and 9D). In the case of co-doping (12.5%), two Zn atoms were replaced by Co and Cu in ZnO NRs:Co/Cu (Figure 9E). The self-consistent iteration was converged to a threshold of 10^{-5} eV/atom. The lattice constants and atomic positions were tuned to maintain a maximum force per atom of 0.03 eV/Å and an internal stress below 0.05 GPa.

We accurately describe the electronic structures by applying the Hubbard U correction to the Zn 3d, O 2p, Cu 3d, and Co 3d states. Based on prior studies,[49–51] a value of Up(O) = 7 eV is suitable for oxidized materials and ensures a realistic treatment of the oxygen 2p orbitals in first-principles calculations. Accordingly, we adopt Ud(Zn) = 10 eV and set Ud = 4 eV for the Cu-3d and Co-3d electrons to account for the localized nature of their d orbitals upon doping. These corrections help improve the accuracy of the electronic structure, especially in capturing the strong on-site Coulomb interactions introduced by transition-metal dopants.

RESOURCE AVAILABILITY

Lead contact

Further information and requests for resources should be directed to and will be fulfilled by the lead contact, M.A. Basyooni-M. Kabatas (m.kabatas@tudelft.nl; m.kabatas@kit.edu).

Materials availability

This study did not generate new, unique materials.

Data and code availability

- The data supporting the findings of this study are available from the lead contact upon reasonable request.
- This study did not generate custom code.
- Any additional information required to reanalyze the data reported in this paper is available from the lead contact upon reasonable request.

ACKNOWLEDGMENTS

The financial support from the EU under the Romanian Recovery and Resilience Plan PNRR, Pillar III, Component C9–I8, contract no. 760083/May 23, 2023, and of the Core Program of the National Institute of Materials Physics, granted by the Romanian Ministry of Research, Innovation, and Digitalization under the project PC1-PN23080101, is acknowledged.

AUTHOR CONTRIBUTIONS

I.B. prepared the samples, performed the experiments and characterization, conducted the data analysis, and wrote the original draft and the revised manuscript. O.E.K. performed the XRD and electrochemical analyses and contributed to writing the original draft and the revised manuscript. I.D. performed the optical measurements. M.A. carried out the DFT calculations and contributed to writing the original draft. M.A.B.-M.K. contributed to characterization, data analysis, and editing. I.E. performed the PL analysis and contributed to the experimental design and supervision of the work. E.M. designed the experiments and supervised the work. All the authors participated in the discussions and commented on the manuscript.

DECLARATION OF INTERESTS

The authors declare no competing interests.

SUPPLEMENTAL INFORMATION

Supplemental information can be found online at https://doi.org/10.1016/j.xcrp.2026.103271.

Received: January 8, 2026
Revised: February 18, 2026
Accepted: April 1, 2026

REFERENCES

1. Sayed, K., Aref, M., Abokhalil, A.G., and Mossa, M.A. (2025). Hybrid and Advanced Energy Storage Systems: Integration, Applications, and Future Trends. In Energy Storage Devices-A Comprehensive Overview, A.Y. Abdelaziz, M.A. Mossa, and M. Bajaj, eds. (IntechOpen).
2. Zhang, Y., Li, Q., Feng, W., Yue, H., Gao, S., Su, Y., Tang, Y., Wu, J., Zhang, Z., Zhang, Y., et al. (2025). Valence Engineering via Polyoxometalate-Induced on Vanadium Centers for Efficient Aqueous Zinc-Ion Batteries. Angew. Chem. *64*, e202501728.
3. Liu, X., Li, W., Guo, X., Su, B., Guo, S., Jing, Y., and Zhang, X. (2025). Advancements in energy-storage technologies: A review of current developments and applications. Sustainability *17*, 8316.
4. Conway, B.E. (2013). Electrochemical Supercapacitors: Scientific Fundamentals and Technological Applications (Springer Science & Business Media).
5. Liang, R., Du, Y., Xiao, P., Cheng, J., Yuan, S., Chen, Y., Yuan, J., and Chen, J. (2021). Transition metal oxide electrode materials for supercapacitors: a review of recent developments. Nanomaterials *11*, 1248.
6. Wu, F., Wang, X., Hu, S., Hao, C., Gao, H., and Zhou, S. (2017). Solid-state preparation of CuO/ZnO nanocomposites for functional supercapacitor electrodes and photocatalysts with enhanced photocatalytic properties. Int. J. Hydrogen Energy *42*, 30098–30108.
7. Das, H.T., Dutta, S., Dutta, S., Das, N., Das, P., Mondal, A., and Imran, M. (2022). Recent trend of CeO2-based nanocomposites electrode in supercapacitor: A review on energy storage applications. J. Energy Storage *50*, 104643.
8. Libich, J., Máca, J., Vondrák, J., Čech, O., and Sedlaříková, M. (2018). Supercapacitors: Properties and applications. J. Energy Storage *17*, 224–227.

9. Rana, A., Malik, R., Rana, M., Kaushik, D., Khanna, S.P., Srivastava, R., and Suman, C.K. (2024). Studies of optoelectrical properties of Mn-doped ZnO nanostructure for supercapacitor and photodetector applications. J. Alloys Compd. *997*, 174931.

10. Muzaffar, A., Ahamed, M.B., Deshmukh, K., and Thirumalai, J. (2019). A review on recent advances in hybrid supercapacitors: Design, fabrication and applications. Renew. Sustain. Energy Rev. *101*, 123–145.

11. Kumar, Y., Chopra, S., Gupta, A., Kumar, Y., Uke, S.J., and Mardikar, S.P. (2020). Low temperature synthesis of MnO2 nanostructures for supercapacitor application. Mater. Sci. Energy Technol. *3*, 566–574.

12. Dhas, S.D., Maldar, P.S., Patil, M.D., Nagare, A.B., Waikar, M.R., Sonkawade, R.G., and Moholkar, A.V. (2020). Synthesis of NiO nanoparticles for supercapacitor application as an efficient electrode material. Vacuum *181*, 109646.

13. Chaudhary, M., Singh, M., Kumar, A., Gautam, Y.K., Gautam, Y.K., Malik, A.K., Kumar, Y., and Singh, B.P. (2021). Experimental investigation of Co and Fe-Doped CuO nanostructured electrode material for remarkable electrochemical performance. Ceram. Int. *47*, 2094–2106.

14. Grover, S., Kadyan, P., Sharma, S., Sharma, K., and Sharma, R.K. (2023). Synthesis and characterization of polyaniline nanotube supported nanocomposite of RuO2 as electrode material for application in supercapacitor device. Materialia *28*, 101732.

15. Girish, K.M., Lavanya, R., Sowmyshree, N., Jain, K.D., Gurushantha, K., and Ramakrishnappa, T. (2025). Preparation and Electrochemical Properties of Co3O4 as Potential Electrode materials for Supercapacitor and Battery applications. Future Batter *6*, 100071.

16. Jha, D., Somapur, B., Paul, A., Kavitha, C., and Kambhala, N. (2025). Enhanced super capacitance performance of $V_2O_5 \cdot nH_2O$/g-C_3N_4 nanocomposites: Synthesis, characterizations, and electrochemical properties. Mater. Chem. Phys. *332*, 130244.

17. Wang, Y., Xiao, X., Xue, H., and Pang, H. (2018). Zinc Oxide Based Composite Materials for Advanced Supercapacitors. ChemistrySelect *3*, 550–565.

18. Rahmati, A., Balouch Sirgani, A., Molaei, M., and Karimipour, M. (2014). Cu-doped ZnO nanoparticles synthesized by simple co-precipitation route. Eur. Phys. J. Plus *129*, 250.

19. Achehboune, M., Khenfouch, M., Boukhoubza, I., Mothudi, B.M., Zorkani, I., and Jorio, A. (2020). Holmium (Ho)-coated ZnO nanorods: an investigation of optoelectronic properties. J. Mater. Sci. Mater. Electron. *31*, 4595–4604.

20. Nallapureddy, R.R., Pallavolu, M.R., B, H.K., Gutturu, R.R., Merum, D., Yedluri, A.K., and Joo, S.W. (2022). Capsule-shaped calcium and cobalt-doped ZnO electrodes for high electrochemical supercapacitor performance. Int. J. Energy Res. *46*, 14334–14345.

21. Ercay, E., Ersoy, S., Ozcan, M., Misirlioglu, F.B., Gungor, A., Ozarowski, A., Kaya, F., Rostas, A.M., Kaya, C., and Erdem, E. (2025). Enhancing ZnO-based supercapacitors through carbon-induced defect centers. MRS Bull.

22. Arshad, M., Meenhaz Ansari, M., Ahmed, A.S., Tripathi, P., Ashraf, S.S.Z., Naqvi, A.H., and Azam, A. (2015). Band gap engineering and enhanced photoluminescence of Mg doped ZnO nanoparticles synthesized by wet chemical route. J. Lumin. *161*, 275–280.

23. Sahu, J., Kumar, S., Ahmed, F., Alvi, P.A., Dalela, B., Phase, D.M., Gupta, M., and Dalela, S. (2023). Electrochemical and electronic structure properties of high-performance supercapacitor based on Nd-doped ZnO nanoparticles. J. Energy Storage *59*, 106499.

24. Chakraborty, M., Mahapatra, P., and Thangavel, R. (2016). Structural, optical and electrochemical properties of Al and Cu co-doped ZnO nanorods synthesized by a hydrothermal method. Thin Solid Films *612*, 49–54.

25. Bozzini, B., Gianoncelli, A., Mele, C., Abyaneh, M.K., Jezersėk, D., Sgura, I., and Kiskinova, M. (2014). Pulse-Plating of Mn–Cu–ZnO for Supercapacitors: A Study Based on Soft X-ray Fluorescence and Absorption Microspectroscopy. Chemelectrochem *1*, 1161–1172.

26. Ammar, A.U., Bakan-Misirlioglu, F., Aleinawi, M.H., Franzo, G., Condorelli, G.G., Yesilbag, F.N.T., Yesilbag, Y.O., Mirabella, S., and Erdem, E. (2023). All-in-one supercapacitors with high performance enabled by Mn/Cu doped ZnO and MXene. Mater. Res. Bull. *165*, 112334.

27. Karpyna, V., Myroniuk, L., Myroniuk, D., Bykov, O., Olifan, O., Kolomys, O., Strelchuk, V., Bugaiova, M., Kovalchuk, I., and Ievtushenko, A. (2024). Effect of Cobalt Doping on Structural, Optical, and Photocatalytic Properties of ZnO Nanostructures. Catal. Lett. *154*, 2503–2512.

28. Zhao, X.Q., Veintemillas-Verdaguer, S., Bomati-Miguel, O., Morales, M.P., and Xu, H.B. (2005). Thermal history dependence of the crystal structure of Co fine particles. Phys. Rev. B *71*, 024106.

29. Meda, L., and Cerofolini, G.F. (2004). A decomposition procedure for the determination of copper oxidation states in Cu-zeolites by XPS. Surf. Interface Anal. *36*, 756–759.

30. Cuscó, R., Alarcón-Lladó, E., Ibáñez, J., Artús, L., Jiménez, J., Wang, B., and Callahan, M.J. (2007). Temperature dependence of Raman scattering in ZnO. Phys. Rev. B *75*, 165202.

31. Chang, Y.Q., Wang, P.W., Ni, S.L., Long, Y., and Li, X.D. (2012). Influence of Co content on Raman and photoluminescence spectra of Co doped ZnO nanowires. J. Mater. Sci. Technol. *28*, 313–316.

32. Tiwari, N., Doke, S., Lohar, A., Mahamuni, S., Kamal, C., Chakrabarti, A., Choudhary, R.J., Mondal, P., Jha, S.N., and Bhattacharyya, D. (2016). Local structure investigation of (Co, Cu) co-doped ZnO nanocrystals and its correlation with magnetic properties. J. Phys. Chem. Solids *90*, 100–113.

33. Gandhi, V., Ganesan, R., Abdulrahman Syedahamed, H.H., and Thaiyan, M. (2014). Effect of Cobalt Doping on Structural, Optical, and Magnetic Properties of ZnO Nanoparticles Synthesized by Coprecipitation Method. J. Phys. Chem. C *118*, 9715–9725.

34. Shi, S., Yang, Y., Xu, J., Li, L., Zhang, X., Hu, G.-H., and Dang, Z.-M. (2013). Structural, optical and magnetic properties of Co-doped ZnO nanorods prepared by hydrothermal method. J. Alloys Compd. *576*, 59–65.

35. Liqiang, J., Yichun, Q., Baiqi, W., Shudan, L., Baojiang, J., Libin, Y., Wei, F., Honggang, F., and Jiazhong, S. (2006). Review of photoluminescence performance of nano-sized semiconductor materials and its relationships with photocatalytic activity. Sol. Energy Mater. Sol. Cells *90*, 1773–1787.

36. Zeng, H., Duan, G., Li, Y., Yang, S., Xu, X., and Cai, W. (2010). Blue Luminescence of ZnO Nanoparticles Based on Non-Equilibrium Processes: Defect Origins and Emission Controls. Adv. Funct. Mater. *20*, 561–572.

37. Singh, S.C., and Gopal, R. (2012). Drop shaped zinc oxide quantum dots and their self-assembly into dendritic nanostructures: Liquid assisted pulsed laser ablation and characterizations. Appl. Surf. Sci. *258*, 2211–2218.

38. Oba, F., Choi, M., Togo, A., and Tanaka, I. (2011). Point defects in ZnO: an approach from first principles. Sci. Technol. Adv. Mater. *12*, 034302.

39. Achehboune, M., Khenfouch, M., Boukhoubza, I., Derkaoui, I., Leontie, L., Carlescu, A., Mothudi, B.M., Zorkani, I., and Jorio, A. (2022). Optimization of the luminescence and structural properties of Er-doped ZnO nanostructures: effect of dopant concentration and excitation wavelength. J. Lumin. *246*, 118843.

40. Gopalakrishnan, R., and Muthukumaran, S. (2013). Nanostructure, optical and photoluminescence properties of Zn1−xNixO nanoclusters by co-precipitation method. J. Mater. Sci. Mater. Electron. *24*, 1069–1080.

41. Boukhoubza, I., Derkaoui, I., Basyooni, M.A., Achehboune, M., Khenfouch, M., Belaid, W., Enculescu, M., and Matei, E. (2023). Reduced graphene oxide-functionalized zinc oxide nanorods as promising nanocomposites for white light emitting diodes and reliable UV photodetection devices. Mater. Chem. Phys. *306*, 128063.

42. Liu, X.-C., Shi, E.-W., Chen, Z.-Z., Zhang, H.-W., Song, L.-X., Wang, H., and Yao, S.-D. (2006). Structural, optical and magnetic properties of Co-doped ZnO films. J. Cryst. Growth *296*, 135–140.

43. Qiu, X., Li, G., Sun, X., Li, L., and Fu, X. (2008). Doping effects of Co2+ ions on ZnO nanorods and their photocatalytic properties. Nanotechnology *19*, 215703.

44. Polat, İ., Yılmaz, S., Altın, İ., Bacaksız, E., and Sökmen, M. (2014). The influence of Cu-doping on structural, optical and photocatalytic properties of ZnO nanorods. Mater. Chem. Phys. *148*, 528–532.

45. P, C., P, S., V, U.S., Mona, Y., and M, D.R. (2024). Study on the electrochemical performance of Ni-doped ZnO nanorods utilized for the high-performance supercapacitor application. Ionics *30*, 4135–4142.

46. Raza, A., Sayeed, K., Naaz, A., Muaz, M., Islam, S.N., Rahaman, S., Sama, F., Pandey, K., and Ahmad, A. (2024). Green Synthesis of ZnO Nanoparticles and Ag-Doped ZnO Nanocomposite Utilizing *Sansevieria trifasciata* for High-Performance Asymmetric Supercapacitors. ACS Omega, 3c10060. acsomega.

47. Clark, S.J., Segall, M.D., Pickard, C.J., Hasnip, P.J., Probert, M.I.J., Refson, K., and Payne, M.C. (2005). First principles methods using CASTEP. Z. Für Krist. - Cryst. Mater. *220*, 567–570.

48. Blöchl, P.E. (1994). Projector augmented-wave method. Phys. Rev. B *50*, 17953–17979.

49. Wu, H.-C., Peng, Y.-C., and Chen, C.-C. (2013). Effects of Ga concentration on electronic and optical properties of Ga-doped ZnO from first principles calculations. Opt. Mater. *35*, 509–515.

50. Derkaoui, I., Achehboune, M., Boukhoubza, I., El Allam, E.m., El Adnani, Z., Henrard, L., and Rezzouk, A. (2023). Effect of strontium (Sr) doping on the structural, electronic and optical properties of ZnO, by first-principles calculations. Phys. B Condens. Matter *660*, 414903.

51. Achehboune, M., Khenfouch, M., Boukhoubza, I., Derkaoui, I., Mothudi, B.M., Zorkani, I., and Jorio, A. (2022). A DFT study on the electronic structure, magnetic and optical properties of Er doped ZnO: effect of Er concentration and native defects. Comput. Condens. Matter *31*, e00627.